EXTENDED PDF FORMAT
SPONSORED BY
**Travel Grants Available**
AACR Annual Meeting 2014
Application Deadline:
January 31st
>Apply Now
http://www.rndsystems.com

# Topological Phase Transition and Texture Inversion in a Tunable Topological Insulator

Su-Yang Xu *et al.*

*Science* **332**, 560 (2011);
DOI: 10.1126/science.1201607

*This copy is for your personal, non-commercial use only.*

**If you wish to distribute this article to others**, you can order high-quality copies for your colleagues, clients, or customers by clicking here.

**Permission to republish or repurpose articles or portions of articles** can be obtained by following the guidelines here.

***The following resources related to this article are available online at www.sciencemag.org (this information is current as of February 11, 2014 ):***

**Updated information and services,** including high-resolution figures, can be found in the online version of this article at:
http://www.sciencemag.org/content/332/6029/560.full.html

**Supporting Online Material** can be found at:
http://www.sciencemag.org/content/suppl/2011/03/31/science.1201607.DC1.html

A list of selected additional articles on the Science Web sites **related to this article** can be found at:
http://www.sciencemag.org/content/332/6029/560.full.html#related

This article **cites 27 articles**, 4 of which can be accessed free:
http://www.sciencemag.org/content/332/6029/560.full.html#ref-list-1

This article has been **cited by** 2 articles hosted by HighWire Press; see:
http://www.sciencemag.org/content/332/6029/560.full.html#related-urls

This article appears in the following **subject collections:**
Physics
http://www.sciencemag.org/cgi/collection/physics

Downloaded from www.sciencemag.org on February 11, 2014

*Science* (print ISSN 0036-8075; online ISSN 1095-9203) is published weekly, except the last week in December, by the American Association for the Advancement of Science, 1200 New York Avenue NW, Washington, DC 20005. Copyright 2011 by the American Association for the Advancement of Science; all rights reserved. The title *Science* is a registered trademark of AAAS.

# Topological Phase Transition and Texture Inversion in a Tunable Topological Insulator

Su-Yang Xu,[1] Y. Xia,[1] L. A. Wray,[1,2] S. Jia,[3] F. Meier,[4,5] J. H. Dil,[4,5] J. Osterwalder,[5] B. Slomski,[4,5] A. Bansil,[6] H. Lin,[6] R. J. Cava,[3] M. Z. Hasan[1,2,7,8]*

**The recently discovered three-dimensional or bulk topological insulators are expected to exhibit exotic quantum phenomena. It is believed that a trivial insulator can be twisted into a topological state by modulating the spin-orbit interaction or the crystal lattice, driving the system through a topological quantum phase transition. By directly measuring the topological quantum numbers and invariants, we report the observation of a phase transition in a tunable spin-orbit system, $BiTl(S_{1-\delta}Se_{\delta})_2$, in which the topological state formation is visualized. In the topological state, vortex-like polarization states are observed to exhibit three-dimensional vectorial textures, which collectively feature a chirality transition as the spin momentum–locked electrons on the surface go through the zero carrier density point. Such phase transition and texture inversion can be the physical basis for observing fractional charge (±e/2) and other fractional topological phenomena.**

Topological insulators in three dimensions are nonmagnetic insulators with novel surface states that are a consequence of the nontrivial topology of electronic wave functions in the bulk of the materials (*1*–*5*). Their experimental discoveries in Bi-Sb semiconductors, and in $Bi_2Se_3$ and related materials, have led to the exploration of topological quantum phenomena at modest temperatures and without the requirement of any applied magnetic field (*6*–*16*). Current theoretical proposals have suggested such intriguing possibilities as the realization of fractional quasi-particles and the exploitation of the role of spin momentum locking, which leads to quantum phases (such as topological Berry's phases), in transport (*17*–*24*).

Strong topological insulators are distinguished from ordinary insulators by a finite topological quantum number or an invariant ($\nu_0$) or, equivalently, an axion angle parameter ($\theta$). The value of $\nu_0$ or $\theta$ depends on the parity eigenvalues of the wave functions in time reversal–symmetric materials (*1*, *2*) and can be determined from spin texture details of the spin-orbit surface states that form when the bulk is terminated, as demonstrated by Hsieh *et al.* (*6*–*9*). In particular, a $\nu_0 = 1 = \theta/\pi$ topology requires the terminated surface to have a Fermi surface that supports a nonzero Berry's phase (an odd as opposed to an even multiple of $\pi = \theta =$ axion angle), which is not realizable in an ordinary spin-orbit or trivial ($\nu_0 = 0 = \theta$) insulator. It is believed that a trivial insulator can be twisted into a $\nu_0 = 1 = \theta/\pi$ topological state by signaling the appearance of unusual spin vortex–like [or skyrmion-like (*1*)] arrangements via increasing spin-orbit interaction or by modulating the lattice parameters, thereby driving the system through a topological quantum phase transition (*1*, *2*). However, the topological insulators $Bi_2X_3$ (X = Se,Te) cannot be tuned out from a trivial insulator version without a structural phase transition; in the Bi-Sb semiconductors, the topological phase transition is masked by an intervening band [the "H" band (*1*)] and the lack of gating control necessary for its observation.

We demonstrate the existence of a topological phase transition in $TlBi(S_{1-\delta}Se_{\delta})_2$, which, as we show, is a fully tunable topological analog of $Bi_2Se_3$. By effectively varying the sulfur/selenium ratio ($\delta$), both the spin-orbit strength and lattice parameters are effectively tuned (*25*). Because the topological order in $TlBi(S_{1-\delta}Se_{\delta})_2$ originates from Bi and Se atoms, and to illustrate an analogy with the known topological insulator $Bi_2Se_3$ (*6*, *8*, *11*), we rewrite the formula as $BiTl(S_{1-\delta}Se_{\delta})_2$. Figure 1A presents systematic photoemission measurements of electronic states that lie between a pair of time reversal–invariant points or Kramers' points ($\bar{\Gamma}$ and $\bar{M}$) obtained for a series of compositions of the spin-orbit material $BiTl(S_{1-\delta}Se_{\delta})_2$. As the selenium concentration is increased, the low-lying bands, separated by a gap of energy 0.15 eV at $\delta = 0.0$, are observed to approach each other; the gap decreases to less than 0.05 eV at $\delta = 0.4$. Both bands demarcating the gap show three-dimensional (3D) dispersion where binding energies vary with momentum perpendicular to the surface, $k_z$ [as probed via varying incident photon energy (*25*)], and roughly correspond to the expected position for the valence and conduction bands. The absence of surface states within the bulk gap suggests that the compound is topologically trivial ($\nu_0 = 0 = \theta$) within a composition range of $\delta = 0.0$ to 0.4. Starting from $\delta = 0.6$, a linearly dispersive band connecting the bulk conduction and valence bands emerges, which threads across the bulk band gap. Incident photon energy modulation studies support the assignment of these Dirac-like bands as originating from the surface (*25*). Moreover, the band continua in the composition range of $\delta = 0.0$ to $\delta = 0.4$ are degenerate, whereas the Dirac-like bands at $\delta = 0.6$ and beyond are spin-polarized (see Figs. 2, 3, and 4).

The system enters a topologically nontrivial phase upon the occurrence of an electronic phase transition between $\delta = 0.4$ and $\delta = 0.6$ at temperatures below 15 K. Although the system approaches the transition from the conventional or no-surface-state side ($\delta = 0.4$), both energy dispersion and Fermi surface mapping (Fig. 1, A and B, for $\delta = 0.4$) show that at the outer boundary of the bulk conduction band continuum that corresponds to the loci where the Dirac surface states would eventually develop, the spectral weight becomes much more intense; however, the surface remains gapped at $\delta = 0.4$, which suggests that the material is still on the trivial side. Finer control of bulk compositional variation does not allow us to locate a precise value for the transition; this could also be a consequence of an intrinsically broader topological transition. A critical signature of a topological phase transition is that the material turns into an indirect bulk band gap material, as conjectured previously (*1*). As $\delta$ varies from 0.0 to 1.0 (Fig. 1C), the dispersion of the valence band evolves from a single-peak to a dual-peak shape with a "dip" at the $\bar{\Gamma}$ point ($k = 0$); the $\delta = 0.0$ compound features a direct band gap in its bulk, whereas the $\delta = 1.0$ compound has a slightly indirect gap. The overall experimental evolution of the spin-orbit ground state is shown in Fig. 2A.

Now we systematically study the end product of the transition, $BiTl(S_0Se_1)_2$, and explore its spin and polarization properties far away from the Dirac node where nonlinear spin-orbit terms are also important. Such terms correspond to analogs of cubic and higher-order Dresselhaus effects arising from the symmetry of the crystal potential. Without these effects, the surface states form a cone that is isotropic in momentum space ($k_x$, $k_y$) and hence generates a circular Fermi contour (*2*). Spins tangentially arranged on such a circular Fermi surface lead to a Berry's phase of $\pi$, which is also a measure of the topological invariant and the axion angle ($\nu_0 = 1 = \theta/\pi$) of the system (*1*, *4*, *6*). However, the details of the symmetry and bulk crystal potential can strongly deform the surface states from that of a circle. We explored

---

[1] Joseph Henry Laboratory of Physics, Department of Physics, Princeton University, Princeton, NJ 08544, USA. [2] Advanced Light Source, Lawrence Berkeley National Laboratory, Berkeley, CA 94305, USA. [3] Department of Chemistry, Princeton University, Princeton, NJ 08544, USA. [4] Swiss Light Source, Paul Scherrer Institute, CH-5232 Villigen, Switzerland. [5] Physik-Institute, Universität Zürich-Irchel, CH-8057 Zürich, Switzerland. [6] Department of Physics, Northeastern University, Boston, MA 02115, USA. [7] Princeton Institute for Science and Technology of Materials, Princeton School of Engineering and Applied Science, Princeton University, Princeton, NJ 08544, USA. [8] Princeton Center for Complex Materials, Princeton University, Princeton, NJ 08544, USA.

*To whom correspondence should be addressed. E-mail: mzhasan@princeton.edu

the Fermi contour of BiTl(S$_0$Se$_1$)$_2$ over a large energy range. This sample features an almost perfectly hexagonal Fermi surface at its native (as-grown) Fermi level (binding energy $E_B = 0.01$ eV), whereas the constant energy contour reverts to isotropic circular shapes when approaching the Dirac node ($E_B = 0.25$ eV and $E_B = 0.50$ eV). A more extreme example is n-type bulk doped Bi$_2$Te$_3$, a topological insulator that features a highly warped concave-in snowflake-shaped Fermi surface because of its large $k_F$ and a small band gap (*25*). To understand the relationship between these Dirac cone deformations and the topological invariants and axion angles ($\nu_0$ and $\theta$), we used spin–angle-resolved photoemission spectroscopy (spin-ARPES) (*26*, *27*). Such spin-resolved study is also critical because Hall transport data are now possible that rely heavily on surface state topology and spin configuration data for interpretation (*15*).

We have carried out spin polarization texture measurements over a large range of binding energies to capture the nonlinear regime that can be accessed by gating for transport measurements. For simplicity, we show results for the hexagonal Fermi surface above the Dirac node and one of the circular Fermi surfaces below the Dirac node of BiTl(S$_0$Se$_1$)$_2$ (Fig. 2, B and E). Figure 2F shows the measured out-of-plane spin polarization ($Pz$) of cuts C and E (binding energy and momentum direction are defined in Fig. 2, D and E, respectively). No significant out-of-plane spin polarization component is observed within the experimental resolution for cuts such as these. The in-plane measurements, on the other hand, show large polarization amplitudes (Fig. 3A), suggesting that the spin texture is mostly 2D. On the basis of these data, we determine the direction of full 3D spin vectors following a two-step routine (*25*, *28*). Because $P_z = 0$ (Fig. 2F), the out-of-plane polar angles are all close to 90°, so only in-plane azimuthal angles are shown in Fig. 3B. On the hexagonal Fermi contour located above the Dirac node (Fig. 3B), the spin vectors obtained from the polarization measurements show that the ground state features a 2D in-plane left-handed chirality spin vortex (a skyrmion in momentum space; Fig. 3, B and C). The direction of the spin is roughly perpendicular to the momentum space track that connects the $\bar{\Gamma}$ point and the momentum point location of the spin on the Fermi surface, rather than being tangential to the Fermi contour, as would be expected for an ideal Dirac cone. Our data also show that the spin texture below the Dirac node is also vortex-like but features right-handed chirality. Therefore, when the system is chemically tuned through the zero carrier density (Dirac node), the chirality of the spin vortex gets inverted, as seen in the data. A systematic method of surface chemical potential tuning has been demonstrated in (*6*) and is also applicable here (*25*). However, it is not physically possible to realize this chirality inversion or chemical tuning in Bi$_2$Te$_3$, because the node is buried under other bands.

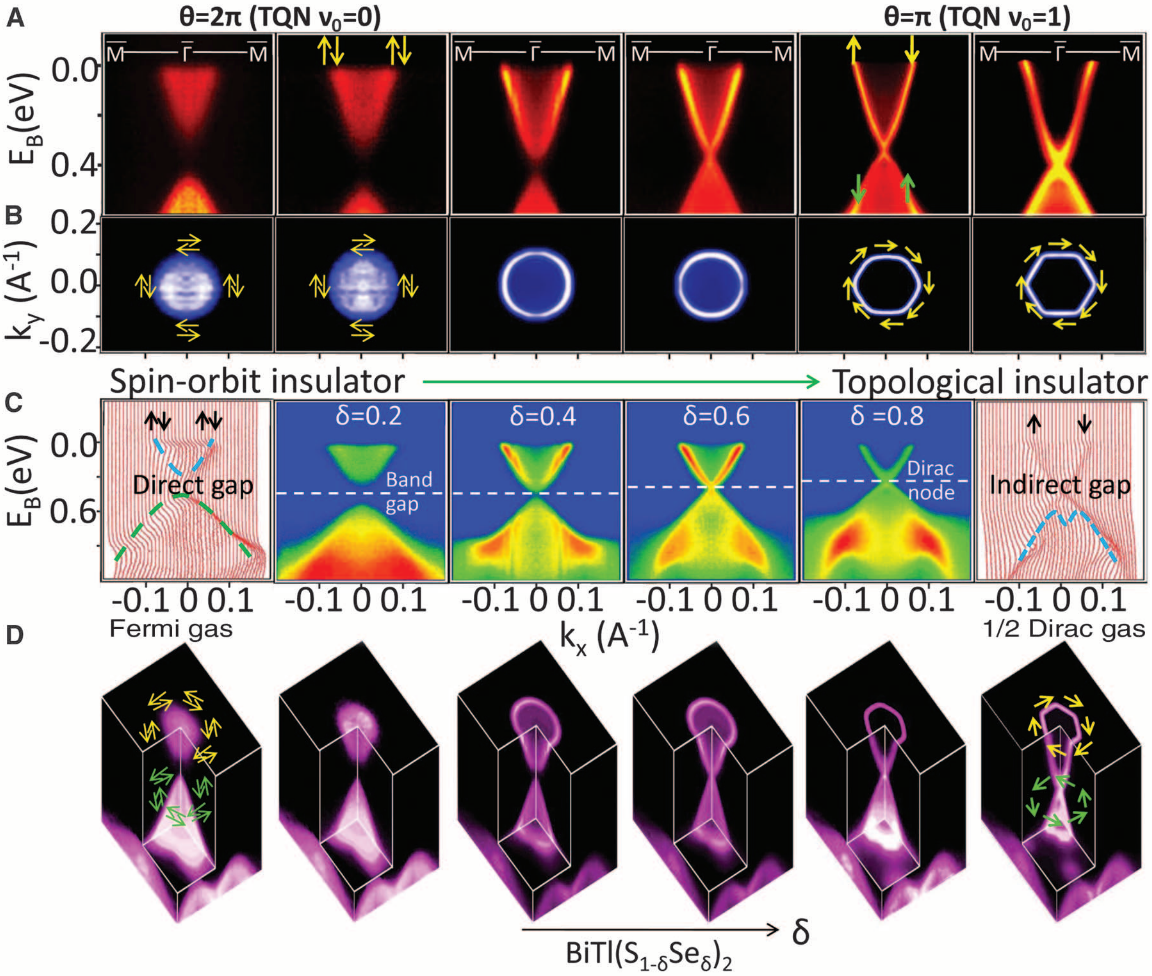

**Fig. 1.** Topological phase transition. (**A**) High-resolution ARPES dispersion maps along the $\bar{\Gamma}$-$\bar{M}$ momentum space line, from a spin-orbit band insulator (left panel) to a topological insulator (right panel). Band insulators and topological insulators are characterized by $\theta = 2\pi$ and $\theta = \pi$, respectively. Topological quantum numbers (TQN) are denoted by topological invariant $\nu_0$. (**B**) ARPES-mapped native Fermi surfaces for different chemical compositions (from left to right, $\delta = 0$ to $\delta = 1$). (**C**) Left and right panels: Energy distribution curves for stoichiometric compositions $\delta = 0$ and $\delta = 1$, respectively. Center panels: ARPES spectra indicating band gap and Dirac node for compositions $\delta = 0.2$ to $\delta = 0.8$. (**D**) Evolution of electronic ground state (3D band topology) imaged over a wide range of energy (vertical axis), spin (arrows), and momentum (horizontal plane). Spin textures are indicated by yellow arrows above the Dirac node and green arrows below the Dirac node. Each arrow represents the net polarization direction on a *k*-space point on the corresponding Fermi surface.

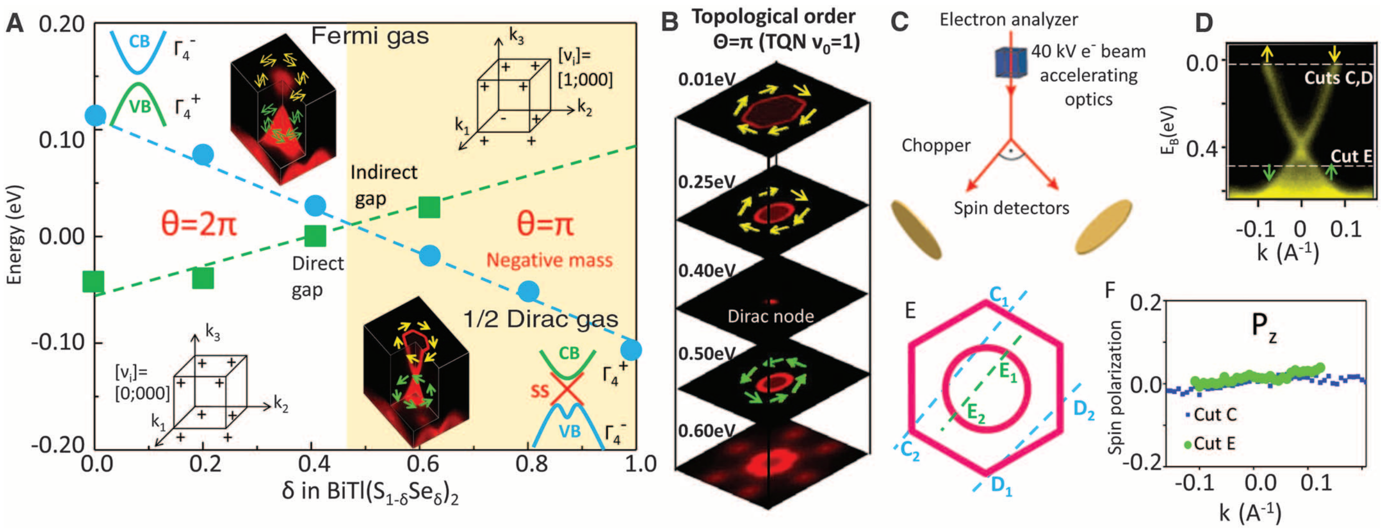

**Fig. 2.** Evolution of spin-orbit ground state and spin texture. (**A**) Energy levels of $\Gamma_4^-$ (blue circles) and $\Gamma_4^+$ (green squares) bands, obtained from ARPES measurements as a function of composition δ. CB, conduction band; VB, valence band. Parity eigenvalues (+ or –) of Bloch states (*25*) are shown. The topological invariants, $\nu_i$, obtained from the parity eigenvalues are presented as $[\theta/\pi = \nu_0; \nu_1\nu_2\nu_3]$ where $\theta = \pi\nu_0$ is the axion angle and $\nu_0$ is the strong invariant (*1*–*4*). (**B**) Fermi surface topology evolution of $BiTl(S_0Se_1)_2$ across the Dirac node. The corresponding binding energies of constant-energy contours are indicated. Observed spin textures are schematically indicated by arrows. (**C**) Experimental scattering geometry used to measure the spin polarization components shown in (B). (**D**) ARPES-measured dispersion along the $\bar{\Gamma}$-$\bar{M}$ momentum space cut. The binding energies used for the cuts are as follows: $E_B$ (cuts C and D) = 0.01 eV, $E_B$ (cut E) = 0.50 eV. (**E**) A map of the momentum space cuts C, D, and E across the Fermi surfaces for the spin polarization measurements. The hexagonal Fermi surface is located 0.40 eV above the spin degenerate node; the circular Fermi surface is located 0.1 eV below the spin degenerate node. (**F**) Measured out-of-plane spin polarization profile of cuts C and E, showing only weak modulations.

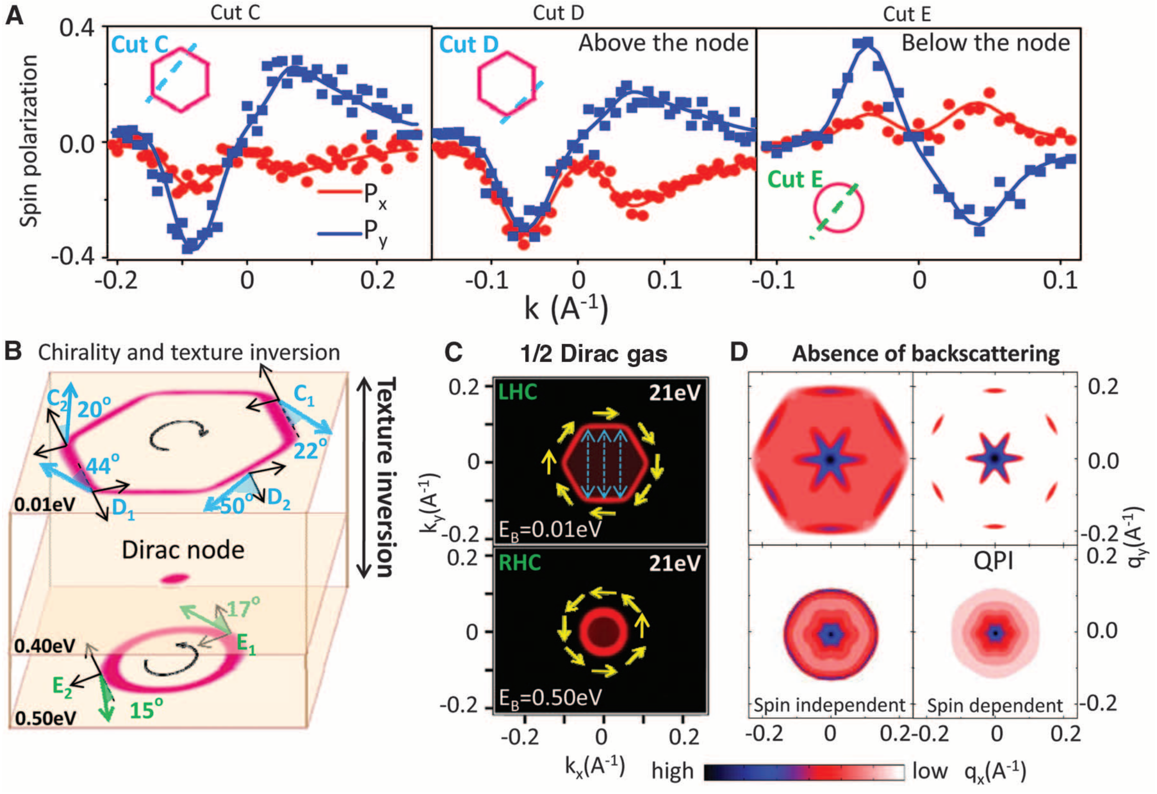

**Fig. 3.** Chirality inversion and spin-dependent scattering profiles for charge and spin transport. (**A**) Measured in-plane spin polarization profiles of cuts C, D, and E (Fig. 2). (**B**) Fitted in-plane azimuthal angle values of spin vectors measured along cuts C, D, and E on the ARPES-measured Fermi surfaces. Spin rotation handedness or chirality changes from left-handed (LHC) to right-handed (RHC) in passing through the Dirac node toward the higher binding energy. The binding energies are indicated at the lower left corner for the experimental Fermi surfaces presented. (**C**) ARPES-measured Fermi surfaces are shown with spin directions based on polarization measurements. Photon energy used for spin-resolved measurements is indicated at the upper right corners. Spin texture reveals a 1/2 Dirac gas. (**D**) Left panels: Spin-independent scattering profiles on Fermi surfaces in (C); right panels: Spin-dependent scattering profiles on Fermi surfaces in (C) relevant for surface quasi-particle transport, which is sampled by the quasi-particle interference (QPI) modes.

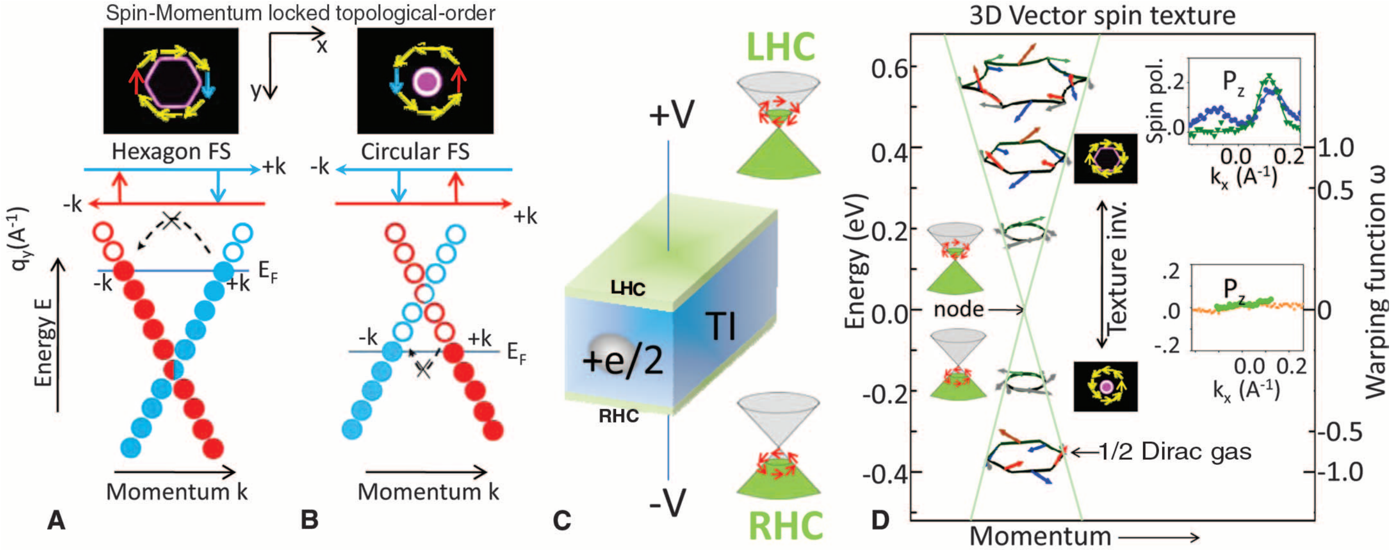

**Fig. 4.** Inversion of spin momentum–locking profile and spin texture phase diagram. (**A** and **B**) A 180° turnaround of the spin momentum–locking profile is observed when chemical potential moves across the Dirac node. In the present experiment, this is equivalent to measuring the profile above and below the Dirac node. The profiles above and below the Dirac node are shown in (A) and (B), respectively. (**C**) A capacitor-like device geometry, using topological insulator thin films of opposite chirality (LHC and RHC) composite, is predicted to host exotic exciton properties where quasi-particle excitation carries fractional charge. (**D**) Spin texture evolution of topological surface bands as a function of energy away from the Dirac node (left axis) and geometrical warping factor ω (right axis). The warping factor is defined as

$$\omega = \frac{k_F(\bar{\Gamma}-\bar{M}) - k_F(\bar{\Gamma}-\bar{K})}{k_F(\bar{\Gamma}-\bar{M}) + k_F(\bar{\Gamma}-\bar{K})} \times \frac{2+\sqrt{3}}{2-\sqrt{3}}$$

where $\omega = 0$, $\omega = 1$, and $\omega > 1$ imply circular, hexagonal, and snowflake-shaped Fermi surfaces, respectively. The sign of ω indicates texture chirality for LHC (+) or RHC (–). The insets show out-of-plane 3D spin polarization measurements at corresponding Fermi surfaces.

The observed chirality inversion of the surface spin texture indicates a 180° turnaround of the spin momentum–locking profile in moving chemical potential across the Dirac node (Fig. 4, A and B). Above the Dirac node, a quasi-particle moving in the $+k$ ($+\hat{x}$) direction is locked with $+\hat{y}$ spin polarization state, whereas below the node, the $+k$ moving quasi-particle state is locked with $-\hat{y}$ spin. These spin polarization states locked to specific momentum states open up many new possibilities for electrical manipulation of spin in a topological device. Manipulation of the Fermi level of a topological insulator—for example, through electrical gating, band structure engineering, or chemical doping–induced gating (*6*, *14*, *29*)—would allow direct observation of the consequences of chirality inversion in the quasi-particle dynamics and interference (Fig. 3).

One particularly interesting proposal involves electrical or chemical gating of both top and bottom surfaces of a topological insulator thin film, resulting in a left-handed chirality (LHC) electron-like Fermi surface on the top and a right-handed chirality (RHC) hole-like Fermi surface of Dirac surface states on the bottom. The interaction between LHC and RHC surface states will lead to excitons at low temperatures with topological properties; the detection of such excitons would allow measurement of the topologically protected fractionalized charge of ±e/2, which can be implemented by optical methods on a device that incorporates the texture inversion (*17*) possible within this materials class (Fig. 4).

To show how these spin textures are relevant in understanding and interpreting quasi-particle transport, such as that observed in the anomalous Hall experiments (*15*) involving the topological insulator surfaces, we explore the key scattering processes on the hexagonal and circular Fermi surfaces observed in our data. Scattering profiles (Fig. 3D) estimated on the basis of the measured spin-ARPES Fermi surfaces and the topological spin textures of $\mathrm{BiTl(S_0Se_1)_2}$ yield the probability of an electron being scattered in momentum transfer (scattering vector) **q** space (*25*, *30*–*32*). Scattering vector **q** is defined as the momentum transfer from one point on a Fermi surface ($|\overline{k}_{\mathbf{F}_1}\rangle$) to another ($|\overline{k}_{\mathbf{F}_2}\rangle$); thus, $\mathbf{q} = |\overline{k}_{\mathbf{F}_2}\rangle - |\overline{k}_{\mathbf{F}_1}\rangle$. We consider the spin texture at a particular binding energy and estimate the spin-independent and spin-dependent scattering profiles (Fig. 3D). The resulting spin-dependent scattering shows a suppression of elastic backscattering on the $\mathrm{BiTl(S_0Se_1)_2}$ surface consistent with its topological order (*25*). Interestingly, for the hexagonal case, a six-fold symmetric quasi-particle scattering profile is seen, indicating the possibility for a fluctuating spin density wave–type magnetic instability that connects the parallel pieces of the observed spin-polarized Fermi surface (Fig. 3, C and D). This surface magnetic instability is expected to contribute strong fluctuations in the spin transport channel. A recent paper based on mean-field Zener theory showed that a helical magnetic order (HMO) is expected if the surface state topology is in the 3D vectorial spin texture (Fig. 4D) regime; the system can then achieve unusually high critical temperature, even up to $T_{\mathrm{HMO}} \approx 100$ K (*30*). Topological quantization in such a system might then survive at a temperature several orders of magnitude higher than in conventional quantum Hall systems.

### References and Notes

1. M. Z. Hasan, C. L. Kane, *Rev. Mod. Phys.* **82**, 3045 (2010).
2. L. Fu, C. L. Kane, E. J. Mele, *Phys. Rev. Lett.* **98**, 106803 (2007).
3. J. E. Moore, *Nat. Phys.* **5**, 378 (2009).
4. X.-L. Qi, T. L. Hughes, S.-C. Zhang, *Phys. Rev. B* **78**, 195424 (2008).
5. M. Z. Hasan, H. Lin, A. Bansil, *Physics* **2**, 108 (2009).
6. D. Hsieh *et al.*, *Nature* **460**, 1101 (2009).
7. D. Hsieh *et al.*, *Science* **323**, 919 (2009).
8. Y. Xia *et al.*, *Nat. Phys.* **5**, 398 (2009).
9. D. Hsieh *et al.*, *Nature* **452**, 970 (2008).
10. S. V. Eremeev, Y. M. Koroteev, E. V. Chulkov, *JETP Lett.* **91**, 594 (2010).
11. H. Lin *et al.*, *Phys. Rev. Lett.* **105**, 036404 (2010).
12. T. Sato *et al.*, *Phys. Rev. Lett.* **105**, 136802 (2010).
13. Y. L. Chen *et al.*, *Phys. Rev. Lett.* **105**, 266401 (2010).
14. L. A. Wray *et al.*, *Nat. Phys.* **6**, 855 (2010).
15. D.-X. Qu, Y. S. Hor, J. Xiong, R. J. Cava, N. P. Ong, *Science* **329**, 821 (2010); 10.1126/science.1189792.
16. J. Chen *et al.*, *Phys. Rev. Lett.* **105**, 176602 (2010).
17. B. Seradjeh, J. E. Moore, M. Franz, *Phys. Rev. Lett.* **103**, 066402 (2009).
18. N. Bray-Ali, L. Ding, S. Haas, *Phys. Rev. B* **80**, 180504 (2009).
19. J. Linder, Y. Tanaka, T. Yokoyama, A. Sudbø, N. Nagaosa, *Phys. Rev. Lett.* **104**, 067001 (2010).
20. L. A. Wray *et al.*, *Nat. Phys.* **7**, 32 (2011).
21. D. Pesin, L. Balents, *Nat. Phys.* **6**, 376 (2010).
22. M. Kargarian, J. Wen, G. A. Fiete, http://arxiv.org/abs/1101.0007 (2011).
23. W. Witczak-Krempa, T. Choy, Y. Kim, *Phys. Rev. B* **82**, 165122 (2010).
24. Y. L. Chen *et al.*, *Science* **329**, 659 (2010).
25. See supporting material on *Science* Online.
26. M. Hoesch *et al.*, *J. Electron Spectrosc. Relat. Phenom.* **124**, 263 (2002).
27. J. H. Dil, *J. Phys. Condens. Matter* **21**, 403001 (2009).

28. Y. Xia *et al.*, http://arxiv.org/abs/0812.2078 (2008).
29. T. Ohta, A. Bostwick, T. Seyller, K. Horn, E. Rotenberg, *Science* **313**, 951 (2006).
30. J. H. Jiang, S. Wu, http://arxiv.org/abs/1012.1299v2 (2010).
31. P. Blaha, K. Schwarz, G. Madsen, D. Kvasnicka, J. Luitz, Computer Code WIEN2K (Vienna University of Technology, 2001).
32. P. Roushan *et al.*, *Nature* **460**, 1106 (2009).

33. We acknowledge discussions with M. Neupane, D. Huse, and D. Haldane. Synchrotron x-ray–based measurements are supported by the Office of Basic Energy Sciences, U.S. Department of Energy (grants DE-FG-02-05ER46200, AC03-76SF00098, and DE-FG02-07ER46352). M.Z.H. acknowledges visiting-scientist support from Lawrence Berkeley National Laboratory and additional support from the A. P. Sloan Foundation. Materials growth and characterization are supported by NSF grant DMR-1006492.

**Supporting Online Material**
www.sciencemag.org/cgi/content/full/science.1201607/DC1
Materials and Methods
SOM Text
Figs. S1 to S18

13 December 2010; accepted 16 March 2011
Published online 31 March 2011;
10.1126/science.1201607

---

# Orbital-Independent Superconducting Gaps in Iron Pnictides

**T. Shimojima,[1,2]*† F. Sakaguchi,[1] K. Ishizaka,[1,2] Y. Ishida,[1,3] T. Kiss,[1] M. Okawa,[1] T. Togashi,[4] C.-T. Chen,[5] S. Watanabe,[1] M. Arita,[6] K. Shimada,[6] H. Namatame,[6] M. Taniguchi,[6] K. Ohgushi,[1,3] S. Kasahara,[7] T. Terashima,[7] T. Shibauchi,[8] Y. Matsuda,[8] A. Chainani,[4] S. Shin[1,2,3,4]†**

The origin of superconductivity in the iron pnictides has been attributed to antiferromagnetic spin ordering that occurs in close combination with a structural transition, but there are also proposals that link superconductivity to orbital ordering. We used bulk-sensitive laser angle–resolved photoemission spectroscopy on $BaFe_2(As_{0.65}P_{0.35})_2$ and $Ba_{0.6}K_{0.4}Fe_2As_2$ to elucidate the role of orbital degrees of freedom on the electron-pairing mechanism. In strong contrast to previous studies, an orbital-independent superconducting gap magnitude was found for the hole Fermi surfaces. Our result is not expected from the superconductivity associated with spin fluctuations and nesting, but it could be better explained invoking magnetism-induced interorbital pairing, orbital fluctuations, or a combination of orbital and spin fluctuations. Regardless of the interpretation, our results impose severe constraints on theories of iron pnictides.

The high-transition-temperature ($T_c$) superconducting iron pnictides (*1*) of the $BaFe_2As_2$ (Ba122) family exhibit a typical phase diagram (Fig. 1A) in which the parent compound remains metallic through an antiferromagnetic (AF) spin-ordering transition at $T_N$ and a tetragonal-to-orthorhombic structural transition at $T_S$ (*2*, *3*). Both $T_N$ and $T_S$ decrease in a similar fashion upon ion substitution and lead to an emergent dome-shaped superconducting (SC) phase with a high $T_c$ of up to 55 K (*4*). Such high $T_c$s are not expected from a conventional electron pairing through lattice vibrations (*5*). Focusing on the nesting tendency connecting quasi-cylindrical Fermi surfaces (FSs), electron pairing mediated by the AF spin fluctuations has been argued (*6*, *7*).

On the other hand, there is a proposal that orbital ordering (*8*–*10*), which causes inequivalency of the Fe *3d* partial density of states, occurs at $T_S$. This phenomenon could give rise to C2 symmetric physical properties that cannot be expected from only 1% lattice distortion at $T_S$. In particular, inequivalent occupation of the xz and yz orbitals (x, y, and z represent orthorhombic axes) near the Fermi level ($E_F$), as observed by angle-resolved photoemission spectroscopy (ARPES), indicates the potential role of orbital degrees of freedom (*11*). Based on the multiorbital nature of iron pnictides, SC pairing through orbital fluctuations has been proposed (*12*–*15*).

Experimental evidence has favored different SC pairing symmetries. Sign-reversal superconductivity suggested by scanning tunneling microscopy on Fe(Te,Se) (*16*) and inelastic neutron spectroscopy on $(Ba,K)Fe_2As_2$ (*17*) is consistent with the s± wave symmetry expected from spin fluctuations. The robustness of $T_c$ against the impurities in LaFeAs(O,F) (*18*) suggests the s++ wave superconductivity, which may be caused by orbital fluctuations. Such material dependence in pairing symmetry can also arise from the balance of these two pairing mechanisms because a crossover from s± to s++ symmetry may occur, depending on the strengths of microscopic electronic parameters (*12*–*15*). However, to date there has been no experimental evidence for the role of orbital fluctuations on the superconductivity in the pnictides.

The pairing mechanism will be reflected in the momentum dependence of the SC gap properties. Spin fluctuation mechanism predicts strongly orbital-dependent SC gap magnitude (*7*, *19*), but orbital fluctuations should eliminate such orbital dependence (*13*–*15*). Because each FS sheet in iron pnictides has a distinct d-orbital character, probing the FS dependence of the SC gap magnitude will be a crucial test for identifying the contribution of the orbital fluctuations in the electron pairing. Here, we report the FS dependence of the SC gap magnitude of representative iron-pnictide superconductors $BaFe_2(As_{0.65}P_{0.35})_2$ (AsP122) and $Ba_{0.6}K_{0.4}Fe_2As_2$ (BaK122) by using bulk-sensitive laser-ARPES (*20*) [see section 1 of the supporting online material (SOM)].

ARPES, using a fixed photon energy (hν), probes a specific profile of the in-plane FSs perpendicular to the momentum axis along the z direction $k_z$. Especially for AsP122 with strong FS warping, the orbital character depends on the $k_z$ value (*21*). Estimation of $k_z$ value corresponding to 7 eV photons of laser-ARPES is thus necessary for investigating the orbital dependence of the SC gap magnitude. Figure 1B is a schematic of the experimental FS profile along the $k_z$ axis of AsP122 taken from (*22*). Whereas the inner hole FS is almost cylindrical, the outer one gets enlarged toward $k_z = \pi$, consistent with the band calculations (inset of Fig. 1A) (*21*). We used a synchrotron radiation photon source of 10 eV and 7 eV to find this characteristic warping in the inner ($k_{F1}$) and outer ($k_{F2}$) Fermi momenta. As shown in Fig. 1, C and D, separation between $k_{F1}$ and $k_{F2}$ in C was three-fourths of that in D, which indicates that 7 eV photons probe the FS profile at $k_z \sim \pi$ to $1.2\pi$. This estimate of $k_z$ for $h\nu = 7$ eV was also quantitatively confirmed by the comparable FS size obtained by the higher photon energy of 63 eV probing $k_z \sim \pi$ (*22*) (Fig. 1E).

High-resolution laser-ARPES *E*-*k* images for AsP122 (Fig. 2, B and C) are along cut 1 and 2 indicated in Fig. 2A, respectively. Both the inner and middle hole bands were resolved as the two-peak feature in the momentum distribution curve (MDC) near $E_F$ (Fig. 2B), although they are nearly degenerate in Fig. 1, C and D. We could separate three hole bands along cut 1 and 2. The temperature ($T$) dependence of the energy distribution curves (EDCs) at $k_F$ in cut 2 (outer FS) shows the SC gap opening below bulk $T_c$ (Fig. 2D), and the SC gap magnitude Δ was directly extracted from the fitting procedure using a Bardeen-Cooper-Schrieffer (BCS) spectral function (SOM, section 2). This Δ value is in excel-

---

[1] Institute for Solid State Physics (ISSP), University of Tokyo, Kashiwa, Chiba 277-8581, Japan. [2] Japan Science and Technology Agency (JST), Core Research for Evolutional Science and Technology (CREST), Chiyoda-ku, Tokyo 102-0075, Japan. [3] JST, Transformative Research Project on Iron Pnictides, Chiyoda-ku, Tokyo 102-0075, Japan. [4] RIKEN SPring-8 Center, Sayo, Hyogo 679-5148, Japan. [5] Beijing Center for Crystal Research and Development, Chinese Academy of Science, Zhongguancun, Beijing 100190, China. [6] Hiroshima Synchrotron Radiation Center and Graduate School of Science, Hiroshima University, Hiroshima 739-8526, Japan. [7] Research Center for Low Temperature and Materials Sciences, Kyoto University, Sakyo-ku, Kyoto 606-8501, Japan. [8] Department of Physics, Kyoto University, Sakyo-ku, Kyoto 606-8502, Japan.

*Present address: Department of Applied Physics, Graduate School of Engineering, University of Tokyo.

†To whom correspondence should be addressed. E-mail: shimojima@ap.t.u-tokyo.ac.jp (T.S); shin@issp.u-tokyo.ac.jp (S.S.)